

The 1996 Outburst of GRO J1655–40: The Challenge of Interpreting the Multi-wavelength Spectra

R.I. Hynes¹, C.A. Haswell^{1,2}, C.R. Shrader³, W. Chen³, Keith Horne⁴,
E.T. Harlaftis⁴, K. O’Brien⁴, C. Hellier⁵ and R.P. Fender^{1,6,7},

¹*Astronomy Centre, University of Sussex, Falmer, Brighton BN1 9QH*

²*Columbia Astrophysics Laboratory, Columbia University, 538 West 120th Street, New York, NY 10027, USA*

³*Goddard Space Flight Center, Greenbelt, MD 20771, USA*

⁴*School of Physics and Astronomy, University of St. Andrews, North Haugh, St. Andrews, Fife KY16 9SS*

⁵*Department of Physics, Keele University, Keele ST5 5BG*

⁶*Astronomical Institute ‘Anton Pannekoek’, University of Amsterdam, The Netherlands*

⁷*Center for High Energy Astrophysics, Kruislaan 403, 1098 SJ, Amsterdam, The Netherlands*

9 September 2018

ABSTRACT

We report on the results of a multi-wavelength campaign to observe the soft X-ray transient (SXT) and superluminal jet source GRO J1655–40 in outburst using *HST*, *RXTE* and *CGRO* together with ground based facilities. This outburst was qualitatively quite different to other SXT outbursts and to previous outbursts of this source. The onset of hard X-ray activity occurred very slowly, over several months and was delayed relative to the soft X-ray rise. During this period, the optical fluxes *declined* steadily. This apparent anti-correlation is not consistent with the standard disc instability model of SXT outbursts, nor is it expected if the optical output is dominated by reprocessed X-rays, as in persistent low mass X-ray binaries.

Based on the strength of the 2175 Å interstellar absorption feature we constrain the reddening to be $E(B - V) = 1.2 \pm 0.1$, a result which is consistent with the known properties of the source and with the strength of interstellar absorption lines. Using this result we find that our dereddened spectra are dominated by a component peaking in the optical with the expected $\nu^{1/3}$ disc spectrum seen only in the UV. We consider possible interpretations of this spectrum in terms of thermal emission from the outer accretion disc and/or secondary star, both with and without X-ray irradiation, and also as non-thermal optical synchrotron emission from a compact self-absorbed central source. In addition to the prominent He II 4686 Å line, we see Bowen fluorescence lines of N III and O III, and possible P Cygni profiles in the UV resonance lines, which can be interpreted in terms of an accretion disc wind. The X-ray spectra broadly resemble the high-soft state commonly seen in black hole candidates, but evolve through two substates.

Taken as a whole, the outburst dataset cannot readily be interpreted by any standard model for SXT outbursts. We suggest that many of the characteristics could be interpreted in the context of a model combining X-ray irradiation with the limit cycle disc instability, but with the added ingredient of a very large disc in this long period system.

Key words: accretion, accretion discs – binaries: close – stars: individual: Nova Sco 1994 (GRO J1655–40) – ultraviolet: stars – X-rays: stars

1 INTRODUCTION

Soft X-ray transients (SXTs), also referred to as X-ray novae, (Tanaka & Shibazaki 1996) are a class of low-mass X-ray binaries (LMXBs) in which long periods of quiescence,

typically decades, are punctuated by very dramatic X-ray and optical outbursts, often accompanied by radio activity as well. The most promising models for explaining the outbursts invoke the thermal-viscous limit cycle instability previously developed for cataclysmic variables (Cannizzo 1993).

These have met with some success in explaining the properties of the outbursts (Cannizzo, Chen & Livio 1995) but there remain difficulties (e.g. Lasota, Narayan & Yi 1996). Compared to cataclysmic variables, an important effect that must be included in models of SXTs is X-ray irradiation of the disc and/or the secondary star. Irradiation of the disc will change its temperature structure (Tuchman, Mineshige & Wheeler 1990) and may induce delayed reflares (Chen, Livio & Gehrels 1993, Mineshige 1994).

The SXT GRO J1655–40 was discovered in 1994 July when *CGRO* Burst and Transient Source Experiment (BATSE) observed it in outburst at a level of 1.1 Crab in the 20–200 keV energy band (Harmon et al. 1995). Since then it has undergone repeated outbursts to a similar level and shown itself to be a very atypical SXT. The outburst history from 1994–5 has been summarised by Tavani et al. (1996), who draw attention to the contrast between the 1994 outbursts which were radio-loud with apparent superluminal jets observed (Tingay et al. 1995, Hjellming & Rupen 1995) and the 1995 outbursts at a similar X-ray flux as in 1994, but radio-quiet. The optical flux from GRO J1655–40 is not as well documented, but Orosz, Schaefer & Barnes (1995) note that optical brightening does not always accompany X-ray outbursts.

After a period of apparent quiescence from late 1995 to early 1996, GRO J1655–40 went into outburst again in late 1996 April (Remillard et al. 1996). Orosz et al. (1997) observed an optical rise leading the X-ray rise detected by *RXTE* by about 6 days. They suggested that this initial behaviour was consistent with the limit-cycle instability. The subsequent X-ray behaviour, however, was not as expected. The soft X-ray flux (2–10 keV), as followed by the *RXTE* All Sky Monitor (ASM) remained at an approximately constant level for more than 4 months, though with considerable short term variability while the hard X-ray flux (20–200 keV) as monitored by *CGRO* BATSE was observed to rise very slowly, not reaching its peak until 4 months after the initial dramatic increase in the soft flux.

During this period we carried out a series of simultaneous *HST* and *RXTE* visits, backed up by ground based observations and *CGRO* BATSE data. We present here our spectral analysis. A subsequent paper will address timing issues. First we summarise the current state of knowledge on the properties of GRO J1655–40: the context in which we interpret our results.

1.1 System parameters

The system parameters of GRO J1655–40 are the best known of any SXT. They are summarised in Table 1. Hjellming & Rupen (1995) estimate the distance from a kinematic model of the jets to be 3.2 ± 0.2 kpc. We also have a lower limit from observations of the 1420 MHz interstellar absorption (Tingay et al. 1995) of 3.0 kpc and an upper limit of 3.5 kpc obtained by the method of Mirabel and Rodríguez (1994). The latter assumes that we can correctly identify the proper motions of the two jets relative to the central source and then only involves the requirement that these proper motions are produced by material moving at no more than the speed of light. These two constraints support the distance estimate of Hjellming & Rupen. Other parameters are taken from Orosz & Bailyn (1997) who model the quiescent

Table 1. Adopted parameters for GRO J1655–40.

Distance	3.2 ± 0.2 kpc
Period	2.62157 ± 0.00015 d
Mass function	3.24 ± 0.09
Inclination	$69^\circ 50 \pm 0^\circ 08$
Mass ratio	2.99 ± 0.08
Primary mass	$7.02 \pm 0.22 M_\odot$

light curve at a time when the disc is estimated to contribute less than 10 per cent of the V band light. Their deduced mass of $7.02 \pm 0.24 M_\odot$ makes it clear that the compact object in this system is a black hole. We note that an independent parameter determination by van der Hooft et al. (1997) yields values consistent with those of Orosz & Bailyn (1997), although with larger uncertainties.

2 OBSERVATIONS AND DATA REDUCTION

2.1 *HST*

Our spectra were obtained by *HST* on five separate visits from 1996 May 14 to July 22 using the Faint Object Spectrograph (FOS) in RAPID mode (Keyes et al. 1995). Table 2 details the exposures obtained. We use the ephemeris of Orosz & Bailyn (1997) to calculate spectroscopic phases at the midpoint of each exposure.

To examine the spectra, we combined the multiple images produced by the RAPID mode into a single image. In addition, where several images were taken with the same disperser, we took an average weighted by exposure time, rebinning higher substep data where necessary.

There are several regions of our spectra for which source count rates become comparable to those in unexposed regions; we must pay careful attention to these background levels to avoid systematic errors in our calibration. There are actually two issues here. Firstly the FOS detectors are always subject to a particle induced dark count. This is modelled and subtracted by the FOS pipeline data processing software but is generally underestimated by up to ~ 30 per cent (Keyes et al. 1995); the actual amount is a function of geomagnetic position and varies over the course of an exposure. This becomes a problem at the short wavelength end of the PRISM spectra. We correct these cases by measuring the count rate in unexposed regions and rescaling the pipeline’s background to this value on an exposure by exposure basis. When the G160L grating is used to observe a very red source such as GRO J1655–40 there can also be a significant amount of light scattered from higher orders. The pipeline measures the residual count rate in unexposed regions of the detector after subtracting the modelled background and subtracts this residual count from the whole spectrum, i.e. it assumes no variation in count rate with pixel number.

In reality, the excess above the *model* background is likely to be due to a combination of underestimating the background and extra scattered light. We therefore compared the results of the pipeline reduction (which assumes all the excess is due to scattered light with a flat spectrum) to rescaling the model background to the unexposed count

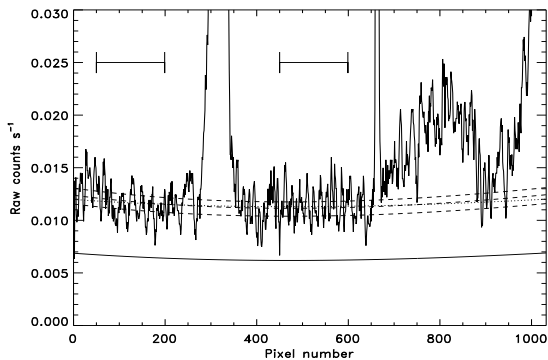


Figure 1. Raw count rates in our first G160L spectrum, over the whole detector, smoothed with a 5 pixel boxcar. We see the zeroth order spectrum centred at pixel 320. The first order spectrum runs from pixels 638–1032. Most prominently we see the geocoronal Ly α emission around pixel 660 and the 2175 Å interstellar absorption feature around pixel 925. We also show with the smooth solid line the model background calculated based upon the geomagnetic position, and with the dashed lines the same scaled up to match the unexposed regions (including our adopted lower and upper limits on this scaling.) The dotted line shows the model background with a fixed (wavelength independent) constant added; it does not differ significantly from the rescaled background. The two adopted unexposed regions are indicated. They span pixels 50–199 and 450–599 respectively.

rate. Since the model background is nearly flat, the differences are small and negligible compared to the uncertainty in the background level. As the excess is much larger for G160L than for other dispersers, for the final analysis we assume that in this case it is dominated by scattered light and accordingly use the pipeline reduction.

We estimate the uncertainty in the background level by examining how the count rate varies between 50 pixel bins over the unexposed region; we are concerned here with real deviations between different parts of the detector, not simply the statistical uncertainty in setting the level of this model. Figure 1 shows one of our raw G160L spectra, together with the pipeline background and our rescaled background.

For the other gratings used there are no unexposed regions in which the background can be checked. The count rate in G400H is much greater than the background for all pixels so this is not an issue. The short wavelength end of the G270H data ($\lesssim 2600$ Å) probably is affected and so should be used with caution. The G190H data is very sensitive to the assumed background for all pixels and disagreed strongly with the G160L data. Since this was only a short exposure, we chose to reject this data.

Spectra obtained using the PRISM have a non-uniform dispersion, which becomes very low at the red end of each spectrum (232 Å per pixel at the far end of the lowest resolution red PRISM spectra). Under these circumstances, a small error in centring the star can lead to a large error in the wavelength and hence flux calibration. In the case of blue PRISM data, comparison with the red PRISM allows us to estimate the point at which this becomes significant; this varies from visit to visit from 2900–4500 Å. For the red PRISM, we do not have any internal checks of the calibra-

tion. We compared our spectra with near simultaneous AAT observations (see Sect. 2.2). The flux levels are consistent to within the intrinsic variability between different nights of the AAT spectra and the shape generally agree well up to ~ 7000 Å. We do see a sharp drop off at the longest wavelengths which we attribute to miscentring, so we adopt cut-offs on a case by case basis ranging from 7300–7650 Å.

For the first visit there were some mismatches at the overlaps of spectra, which could be due to calibration uncertainties (estimated at 5–10 per cent) or intrinsic variability in the source. The blue and red PRISM and G400H data all agreed well, so we took these as a reference and then multiplied the G270H data by 0.92 and the G160L data by 1.06 to ensure consistency in the 3235–3276 Å and 2437–2509 Å regions respectively. As noted above, the relative calibration of G160L and G270H is very uncertain due to the background contribution to the G270H data.

As can be seen from Fig. 1, the G160L spectra show a strong geocoronal Ly α emission feature, with negligible source counts shortwards of this. We therefore ignore data below 1255 Å. We also observe a very weak second order Ly α at 2435 Å and exclude pixels contaminated by this. Finally, we note that the red PRISM data from the first visit (only) showed pronounced a dip from 3735.8–3991.4 Å that was not matched by features in the grating spectra. This region is about 20 pixels wide (the width that would be affected by a single dead diode) so we also exclude these pixels.

We produced a composite PRISM spectrum for each visit together with a separate grating spectrum (for the first visit only) which agrees very well with the PRISM spectrum. The resultant composite spectra are shown in Fig. 2 together with the AAT spectra described in Sect. 2.2.

2.2 Ground based spectroscopy

We observed GRO J1655–40 on the nights of 1996 May 11–13 with the Anglo-Australian Telescope (AAT). These observations formed part of a co-ordinated campaign to observe the variability of GRO J1655–40 with high time resolution optical spectroscopy and X-ray timing with *RXTE* (to appear in a subsequent paper) The RGO spectrograph was used in conjunction with the 270R grating and Tektronix CCD. This gave a mean reciprocal dispersion of 3.4 Å pixel $^{-1}$. Exposure times and wavelength ranges varied over the three nights, due to changes in instrumental set-up. See Table 3.

The spectra were extracted from the raw images with the optimal extraction algorithm of Horne (1986), using suitable fits for the sky lines. The calibration used subroutines within the MOLLY spectroscopic data reduction package. Spectra were wavelength calibrated using 3rd order polynomial fits to CuAr arc calibration spectra. The flux calibration used wavelength dependent fits to tabulated data for the flux star LTT 4364 (Hamuy et al. 1994), including telluric line extinction effects. The final stage of the calibration used wide-slit exposures of the flux star to make an approximate correction for light loss in the object frames due to the narrower slit width used.

We do observe a near linear drop off in the spectra at the longest wavelengths that does not agree well with the *HST* spectra. We interpret this as due to differential refraction moving the red part of the image off the slit and truncate the spectra at 7100 Å accordingly.

Table 2. Log of 1996 *HST* observations of GRO J1655–40. The PRISM was used with both the blue (BL) and red (RD) detector. For the gratings, the resolution, $\lambda/\Delta\lambda$ is about 250 for G160L and 1300 for G190H, G270H, G400H. Spectroscopic phase zero is when the secondary star has maximum positive radial velocity.

Date	Disperser	Start time (UT)	End time (UT)	Integrating time (s)	Midpoint spectroscopic phase	Wavelength range (Å)	Reciprocal Dispersion (Å pixel ⁻¹)
May 14	G190H	00:07:23	00:14:35	365.4	0.35	1573–2330	0.4
	G160L	00:19:50	00:46:58	1574.9	0.36	1138–2507	3.5
	PRISM (BL)	01:42:24	01:47:55	280.0	0.38	1547–5940	–
	G160L	01:53:40	02:23:32	1733.0	0.38	1138–2507	3.5
	G160L	03:18:27	03:36:02	893.2	0.41	1138–2509	1.7
	G160L	03:39:37	03:47:11	438.5	0.41	1138–2507	3.5
	PRISM (BL)	03:52:51	03:58:55	308.5	0.41	1547–5940	–
	G270H	04:56:21	05:10:00	692.9	0.43	2221–3277	0.5
	G400H	06:32:11	06:39:40	379.6	0.46	3235–4781	0.7
PRISM (RD)	08:08:30	08:14:40	313.2	0.48	1621–8849	–	
May 20	<i>Target acquisition failed</i>						
May 27	<i>Target acquisition failed</i>						
June 8	PRISM (RD)	12:48:53	13:06:28	893.2	0.09	1620–8887	–
	PRISM (RD)	14:21:57	15:03:01	2383.2	0.12	1620–8771	–
	PRISM (BL)	16:01:31	16:41:42	2332.2	0.15	1501–5903	–
	PRISM (BL)	17:41:22	18:17:33	2099.9	0.17	1501–5903	–
June 20	PRISM (RD)	11:36:02	11:46:41	617.4	0.65	1620–8771	–
	PRISM (RD)	12:34:59	12:51:35	963.4	0.67	1620–8771	–
	PRISM (RD)	12:55:16	13:12:51	994.9	0.67	1620–8771	–
	PRISM (BL)	14:12:25	14:51:56	2293.8	0.70	1500–5903	–
	PRISM (BL)	15:52:53	16:34:28	2413.1	0.72	1500–5903	–
June 30	PRISM (RD)	13:01:46	13:12:25	617.4	0.49	1620–8771	–
	PRISM (RD)	14:03:31	14:20:07	963.4	0.50	1620–8771	–
	PRISM (RD)	14:23:48	14:41:23	994.9	0.51	1620–8771	–
July 22	PRISM (RD)	07:10:05	07:27:40	893.2	0.79	1620–8887	–
	PRISM (RD)	08:43:07	09:26:23	2511.5	0.81	1620–8771	–

Table 3. Log of AAT spectroscopic observations.

Date	Start time (UT)	Duration (s)	Spectroscopic phase	Useful wavelength range (Å)
May 11	13:34:24	300	0.42	4500–7495
May 12	13:39:44	200	0.81	4498–7947
May 13	13:31:47	500	0.19	3884–7341

2.3 *RXTE* data

We observed GRO J1655–40 with the *RXTE* Proportional Counter Array (PCA) at 6 separate epochs, 4 of which coincide with our *HST* pointings. Table 4 shows the observing log in which we list the start/end time in UT and the duration of the on-source exposure. The total exposure time was 40.74 ks. We obtained data at various time resolutions, as one goal of this program was to search for cross-correlations between rapid variability in optical/UV/X-ray bands.

The PCA, which consists of 5 gas proportional counter modules, provides spectral coverage over the 2–60 keV range. For a complete discussion of the *RXTE* instrumentation see Jahoda et al. (1996). We used two standard PCA data modes together with a 16 energy channel mode binned at 4-ms time resolution and two single channel, single bit modes at 62-

μ s. We constructed spectra from the ‘standard mode’ data with 128 energy channels over the bandpass. Typical count rates were $\sim 10^4$ s⁻¹, so statistical errors were very small. Response matrices and estimated background count spectra were constructed using the standard *RXTE* data analysis procedures. Subsequent spectral analysis then used the XSPEC package distributed by the High Energy Astrophysics Science Archive Research Center (HEASARC).

2.4 *CGRO* data

The BATSE Large Area Detectors (LADs), which were designed for the study of gamma-ray bursts, have been used extensively and with great success to monitor hard-X-ray sources using the earth-occultation technique. Each of the

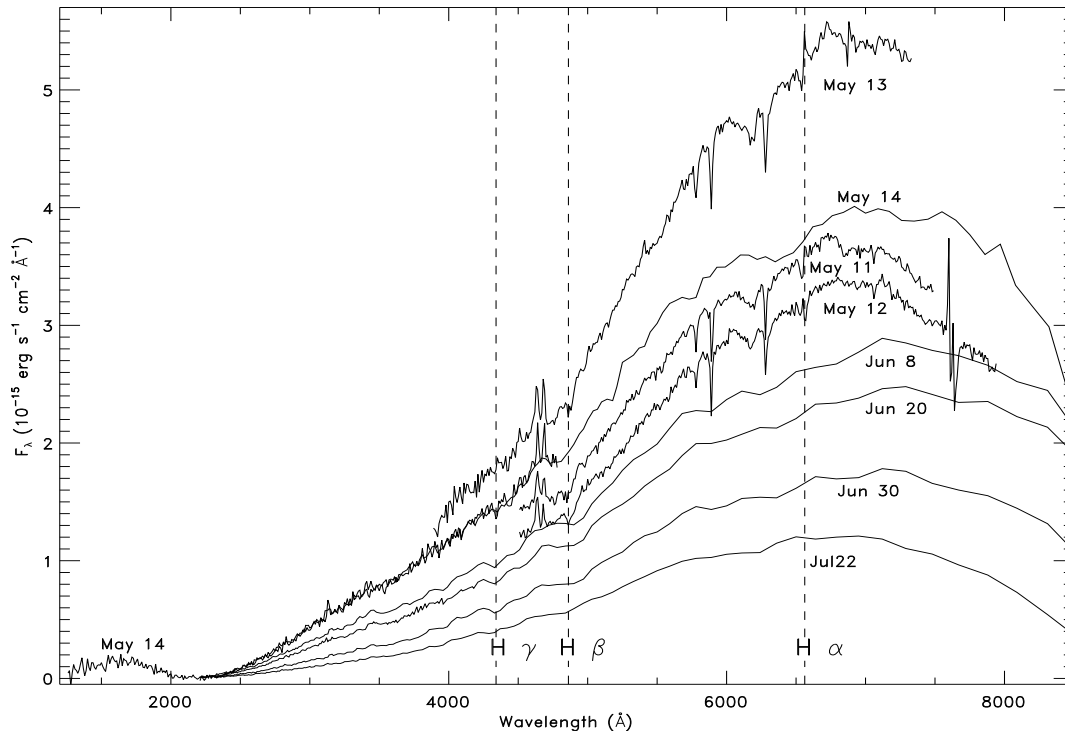


Figure 2. Composite spectra for all *HST* and AAT observations. Spectra have been rebinned to 10 \AA for clarity. The long wavelength data has been retained for comparison here, but was truncated for subsequent analysis. See text for details.

eight LADs, located at the corners of the *CGRO* spacecraft in an octahedral geometry, are unshielded NaI scintillators with a nominal 2π sr field of view with sensitivity over 16 energy channels covering about 20–1900 keV. The data are sampled at 2-second intervals (although the effective time resolution here is ~ 1 90-minute spacecraft orbit). The useful limiting sensitivity of the earth-occultation technique is typically ~ 100 mCrab. For a complete description of this technique and its capabilities see Harmon, et al. (1992). We constructed a light curve, spanning the interval covered by our *HST* and *RXTE* campaign, using the standard earth-occultation data products obtained under the auspices of a *CGRO* Guest Investigator Program designed to study X-ray novae outbursts. The fluxes are derived from summations of typically several days of data within a given viewing period, using the weighted (by viewing angle) average of typically 2–3 LADs. Count rates were converted to photon flux by assuming in this case a photon power-law index, Γ , of 2.8 (where $N(E) \propto E^{-\Gamma}$) and applying an absolute calibration. Energy channels covering approximately 20–200 keV were included in the analysis. The resulting light curve is shown in Figure 3. The vertical axis is equivalent to photons $\text{cm}^2 \text{ s}^{-1}$, with the $0.3 \simeq 1$ Crab as indicated. A nominal threshold is 0.03 photons $\text{cm}^2 \text{ s}^{-1}$.

3 LONG-TERM MULTI-WAVELENGTH EVOLUTION

The general nature of the outburst is characterised by Fig. 3, showing the *CGRO* BATSE (20–200 keV), *RXTE* ASM (2–

12 keV) and *HST* FOS light curves from Spring/Summer 1996. Most striking is the contrast between the optical/UV decline and the slow hard X-ray rise, an apparent anticorrelation. We note that Motch, Ilovaisky and Chevalier (1985) observed a hard–soft transition in the black hole candidate GX 339–4 during 1981 June in which the *soft* X-ray rise was accompanied by an apparently anticorrelated optical decline. The timescales and spectral changes involved in that transition were quite different to those in GRO J1655–40 however, and there is not an obvious connection between the two cases.

Also notable is the difference between the rapid rise in the soft X-ray band, and the delayed, slower rise in the hard X-ray band. This is contrary to at least one other case, X-ray Nova Muscae 1991 where the hard flux rise preceded the soft (Ebisawa et al. 1994). That outburst, however, exhibited a canonical fast-rise, exponential decay light curve (Chen, Shrader & Livio 1997) which was certainly not the case here. Hameury et al. (1997) have successfully modelled both the optical and soft X-ray rise in GRO J1655–40 using a two-component model involving a conventional outer disc and an advective inner disc. In this model, the outburst is triggered by the limit cycle instability acting in the outer disc, but the 6 day soft X-ray delay is due to the need to fill up the inner disc.

Radio detections of this outburst were short-lived; there certainly was not the sustained radio activity, nor the large amplitudes, of the 1994 outburst, and no jets were detected. Hjellming & Rupen (1996) report no detection above 0.5 mJy between 1996 January and May 20. On May 29 they detected GRO J1655–40 at 19 mJy (4.8 GHz) when Hun-

Table 4. Log of *RXTE* spectroscopic observations.

Date	Start/End (UT)	Duration (ks)
May 14	00:07–00:28	1.26
	01:42–02:04	1.32
	03:24–03:40	0.96
May 20	13:55–14:33	2.28
	14:35–14:56	1.26
	15:42–16:09	1.62
	16:11–16:33	1.32
	17:24–17:46	1.32
May 27	17:48–18:09	1.26
	17:29–18:19	3.00
June 8	19:07–19:55	2.88
	12:45–13:41	3.36
June 20	14:21–15:23	3.72
	15:57–17:02	3.90
	17:33–18:34	3.66
	12:55–13:12	1.02
June 30	14:31–14:54	1.38
	16:07–16:35	1.68
June 30	13:00–13:59	3.54

stead & Campbell-Wilson (1996) also detected it at a flux of 55 ± 5 mJy (843 MHz). This flare decayed initially with an e-folding time 1.4 days (Hunstead, Wu & Campbell-Wilson 1997) making it much shorter lived than the activity at other wavelengths. The first detection of this flare is marked in Fig. 3 and appears to coincide with the initial step-like rise in the BATSE light curve. The actual beginning of the flare could have been up to 9 days before this however. This contrasts with the outburst of 1994 when radio flares *followed* hard X-ray outbursts. There also appears to have been an increase in soft X-ray variability at this time; this may be related to the rise of the hard component.

4 INTERSTELLAR EXTINCTION

4.1 Ultraviolet extinction

We use our ultraviolet spectra through the 2175 Å interstellar absorption feature to estimate the reddening. This method assumes that the observed spectra can be fit by a reddened power-law, and has previously been applied to the sources X-ray Nova Muscae 1991 (Cheng et al. 1992) and GRO J0422+32 (Shrader et al. 1994). While the underlying spectrum may not be an exact power-law, this should be a reasonable approximation over the restricted spectral range in which the extinction curve varies rapidly. No other assumptions about the properties of GRO J1655–40 are required, although we do need to assume an extinction curve. We adopt the mean galactic extinction curve of Seaton (1979). The R_V dependent curves of Cardelli, Clayton and Mathis (1989) do yield similar values for the reddening if we assume the average $R_V = 3.2$. We also considered the unusual extinction curve of σ Sco (Clayton & Hanson 1993), which lies 17° from GRO J1655–40. The fit with this curve was significantly poorer than with the S79 curve.

Initial attempts to fit a reddened $f_\nu \propto \nu^{1/3}$ power-law (see Sect. 6.1) to the whole spectrum (Horne et al. 1996) suggested a value of $E(B - V) = 1.3$. This yielded a poor fit to the 2175 Å feature. Examining the dereddened spectra however, we find an intrinsic break around 2600 Å. Analysis of background counts and scattered light in the UV cannot explain this purely as a calibration problem. As this break appears in spectra dereddened with a wide range of parameters, for all extinction curves considered, it is unlikely to be an artefact of the dereddening process. We therefore base our revised reddening estimate on the UV data obtained with the G160L grating only. While both the G270H and PRISMs overlap into the region below 2600 Å, this region is very sensitive to an incorrect background subtraction (more so than the G160L in the overlap region) and so including this data would be more likely to systematically bias our reddening estimate than to improve it.

We fit reddened power-law models to the average G160L spectra by χ^2 minimisation, using a robust grid-search method to locate the minimum. Errors are estimated from 1σ two-parameter confidence intervals as defined by Lampton, Margon & Bowyer (1976). Our estimates are shown in Table 5. They are not sensitive to whether the excess light is taken to be scattered light or particle induced but they are strongly affected by the *level* subtracted. The fit to the spectrum assuming all of the excess to be scattered light, shown in Fig. 4, is extremely good. The dereddened spectra are shown in Fig. 5.

4.2 Direct optical estimation

We can also obtain a direct estimate of the visual extinction, A_V , by considering the expected absolute magnitude of the secondary star. Orosz & Bailyn (1997) obtain a best fit spectral type of F5 IV, with an acceptable range of F3–

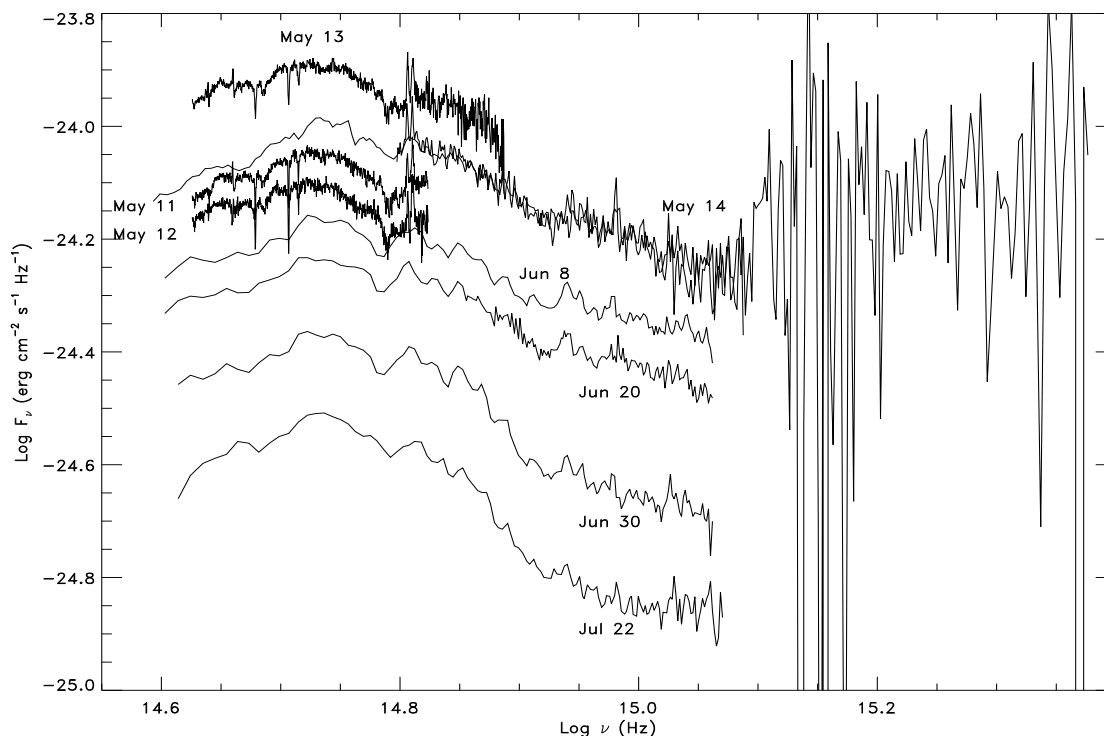


Figure 5. Spectra dereddened using the S79 extinction law with $E(B - V) = 1.2$.

Table 5. Best fits to May 14 UV observations using a power-law spectrum reddened with the galactic average extinction curve. We compare various models for the subtraction of excess light from the UV spectrum in order to assess the systematic uncertainty this introduces. See Fig. 1 for an illustration of the highest and lowest background estimates.

Background model	$E(B - V)$	α	χ_R^2
Pure scattered light, best estimate	1.19 ± 0.07	0.35 ± 0.16	1.10
Pure particle background, best estimate	1.21 ± 0.07	0.47 ± 0.17	1.10
lowest estimate	1.08 ± 0.06	0.57 ± 0.15	1.10
highest estimate	1.34 ± 0.09	0.37 ± 0.19	1.12

F6IV and an effective radius of $4.85 \pm 0.08 R_{\odot}$. Using absolute magnitudes and radii of main sequence F3–F6 stars (Gray 1992) we can rescale the magnitudes to the effective radius of GRO J1655–40 thereby approximating the absolute magnitude of the secondary star to be $M_V = 0.7 \pm 0.5$. Orosz & Bailyn (1997) observe a mean magnitude in quiescence of $m_V = 17.12$ and estimate by fitting photospheric absorption lines that the disc contributes < 10 per cent of the visible light. Assuming a disc contribution of ~ 5 per cent gives a mean apparent magnitude of the secondary star of 17.18 ± 0.06 . The errors in this figure are significantly less than in our estimate of the absolute magnitude. Adopt-

ing a distance of 3.2 ± 0.2 kpc (see Sect. 1.1), we obtain $A_V = 4.0 \pm 0.5$ hence, assuming an average extinction curve ($R_V = 3.2$), $E(B - V) = 1.25 \pm 0.17$. This estimate is dependent on the assumed system parameters, and so vulnerable to systematic errors in these.

4.3 Interstellar absorption lines

In keeping with the highly reddened nature of GRO J1655–40, we see a rich spectrum of interstellar features in our AAT spectra. We measure the equivalent width of the unresolved Na D doublet to be $2.5 \pm 0.1 \text{ \AA}$ and also identify diffuse interstellar bands (Herbig 1995) at 5778/80, 6177 and 6284 \AA . Bianchini et al. (1997) make more precise measurements of the equivalent widths of the Na D doublet (5890 \AA) and the 6613 \AA interstellar band of 2.26 \AA and 0.27 \AA respectively. They deduce $E(B - V) = 1.30$ and 0.97 respectively.

This method should be viewed with caution however. Firstly, Bailyn et al. (1995) obtained a much larger Na D equivalent width of 4.5 \AA at a time when the doublet was blended with He I emission. In spite of this they obtain a *lower* reddening of $E(B - V) = 1.15$ simply by using a different equivalent width–reddening relation. Secondly, as noted by Munari and Zwitter (1997), the Na D-lines are not in general sensitive to $E(B - V) \geq 0.5$ due to saturation, so this method can underestimate the reddening; whether it does or not depends on the detailed substructure of the lines which is not usually resolved.

There may also be signs of the very broad structure (VBS) that has previously been reported in extinction curves of highly reddened objects (Krelowski, Maszkowski

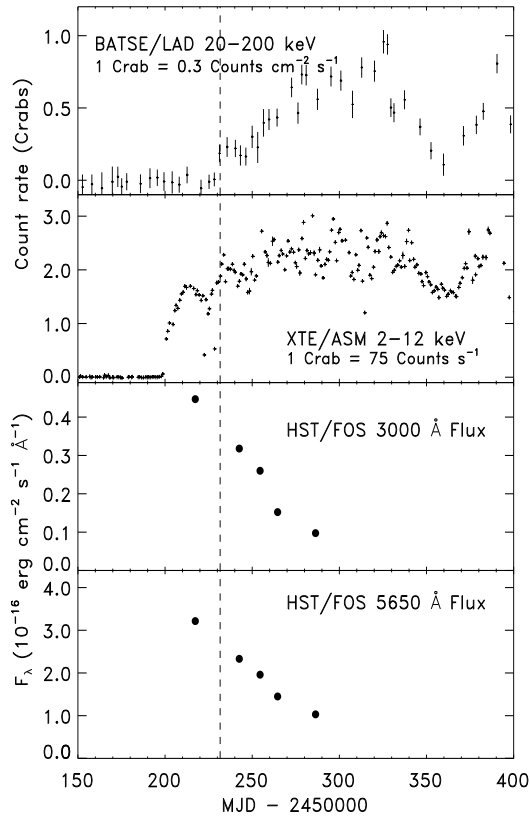


Figure 3. Long term light curves of the 1996 outburst. Statistical errors in the UV and optical points are comparable to or smaller than the symbols used. The time-axis begins at 1996 March 8. The discrepant behaviour of the optical-UV and X-ray data is clear. The dotted line shows the first radio detection of this outburst. The closest non-detection was 9 days before this, making the exact beginning of radio flare difficult to pinpoint.

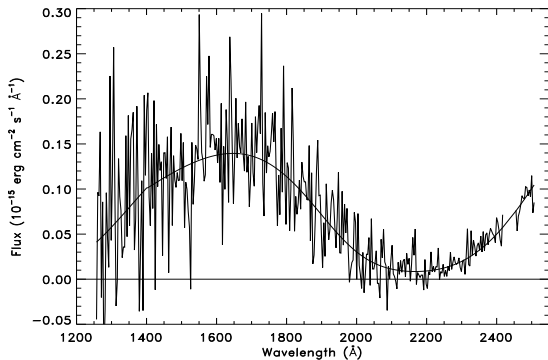


Figure 4. Best fitting reddened power-law to 14 May data assuming all the excess to be scattered light.

& Strobel 1986). This consists of very shallow dips in the extinction curve between 5000 Å and 8000 Å and shows up as apparent weak, broad emission features centred at 5300, 5900 and 6800 Å. We can possibly identify VBS in our spectra, in particular around 6800 Å, (see Fig. 2).

4.4 X-ray absorption

The most precise measurements of the absorption column density are those obtained by fitting *ASCA* spectra. Inoue et al. (1994) derive $N_{\text{H}} = 5 \times 10^{21} \text{ cm}^{-2}$ from observations on 1994 August 23. Subsequent observations obtained $4.4 \times 10^{21} \text{ cm}^{-2}$ (Nagase et al. 1994) and $8 \times 10^{21} \text{ cm}^{-2}$ (Inoue et al. 1995). Greiner, Predahl & Pohl (1995) use the *ROSAT* high-resolution imager to resolve the dust scattering halo. Modelling this they deduce $N_{\text{H}} = 7 \times 10^{22} \text{ cm}^{-2}$.

4.5 Summary

It is encouraging that direct estimates of the visual extinction, measurements of interstellar absorption lines and fitting the 2175 Å feature all give consistent results. We adopt the *HST* value as our best estimate of the reddening: $E(B - V) = 1.2 \pm 0.1$. This can be compared with the extinction maps of the Galactic plane presented by Neckel & Klare (1980). GRO J1655-40 lies close to the boundary of two of their regions, one of low extinction, for which we would expect $E(B - V) \sim 0.4$ at 3.2 kpc, and one of high extinction, for which the highest extinctions measured (up to ~ 2.5 kpc) correspond to $E(B - V) = 1.3$. Our measurement is thus consistent with the position of GRO J1655-40.

Furthermore, using the gas to dust scaling of Bohlin et al. (1978), and their estimate of the scatter in this relationship, this would correspond to a range of hydrogen column densities of $N_{\text{H}} = 4.6 - 10 \times 10^{21} \text{ cm}^{-2}$, in good agreement with the range of *ASCA* values observed. In subsequent analysis we adopt the intermediate *ASCA* measurement of $N_{\text{H}} = 5 \times 10^{21} \text{ cm}^{-2}$, but allow this to vary between $3 - 8 \times 10^{21}$. We ignore the *ROSAT* result as it disagrees with *ASCA*, optical and UV measurements.

5 SPECTRAL LINES

5.1 Ultraviolet resonance lines

We see likely P Cygni profiles in the UV resonance lines: Si III ($\lambda 1302$), Si IV ($\lambda 1397$) and C IV ($\lambda 1549$) together with possible C II ($\lambda 1335$) absorption: Fig. 6a. Although the detection of these is marginal, their positions are correct and the peak to trough separation of all three P Cygni profiles corresponds to velocities of order 5000 km s^{-1} ; comparable to (although somewhat higher than) those seen in dwarf novae in outburst (Shlosman & Vitello 1993 and references therein). Shlosman & Vitello model the expected disc wind profiles in the C IV 1550 line accounting for the non-radial outflow and solving the radiative transfer problem in detail. They find that for low inclination systems where the disc is seen through the wind, only a blue-shifted absorption component is seen. For high inclination systems, symmetric emission is seen from the wind. Only for a relatively narrow range of inclinations

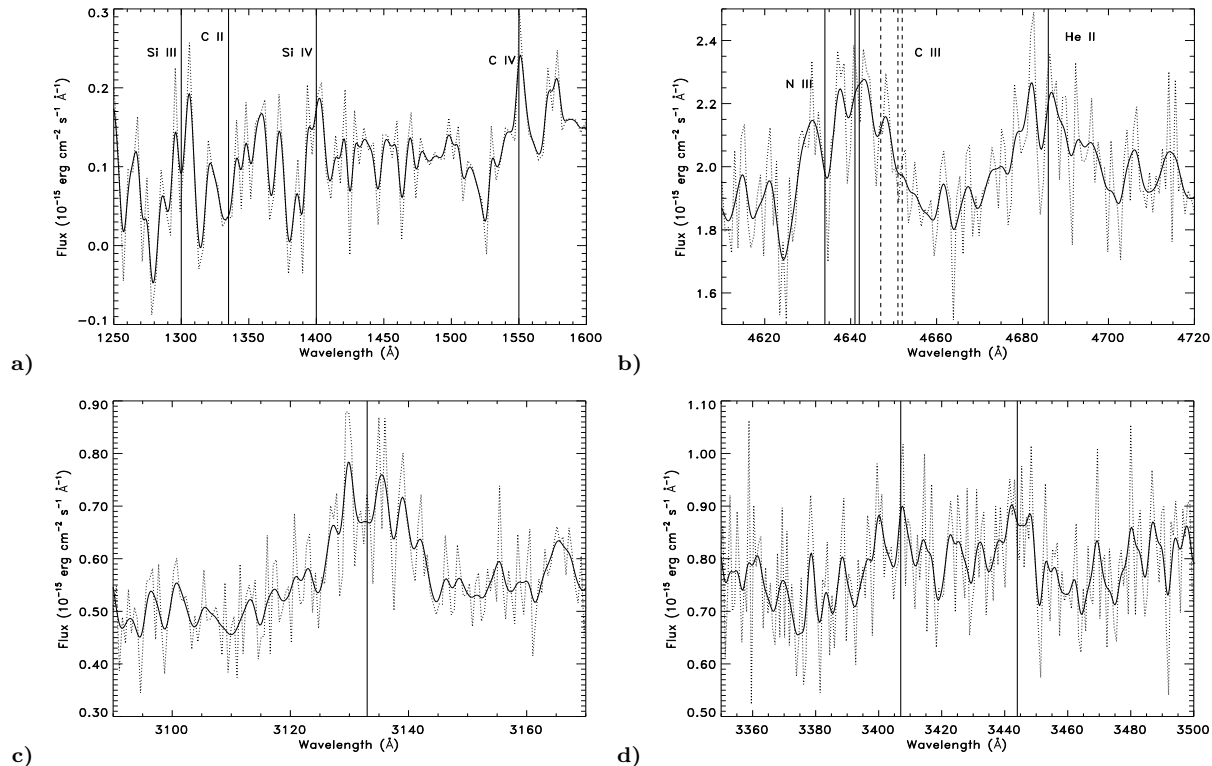


Figure 6. *HST* line profiles. The dotted line shows the raw data; the solid line is the same smoothed with a width equal to a resolution element. a) Possible P Cygni profiles in the UV resonance lines. b) The N III $\lambda\lambda 4634, 4641, 4642$ and He II $\lambda 4686$ emission lines. The positions of the C III $\lambda\lambda 4647, 4651, 4652$ lines are marked with dotted lines. c) The O III $\lambda 3133$ emission line. d) The possible O III $\lambda\lambda 3407, 3444$ emission lines.

Table 6. Properties of emission lines detected in May spectra.

Line	Telescope/ date	Fitted wavelength	Line flux (10^{-15} erg s $^{-1}$ cm $^{-2}$)	EW (Å)	FWHM (Å)
O III($\lambda 3133$)	<i>HST</i> /May 14	3133.2 ± 0.7	2.9 ± 0.4	5.6 ± 0.8	14 ± 2
O III($\lambda 3407$)	<i>HST</i> /May 14	3405.0 ± 2.6	2.6 ± 0.9	3.5 ± 1.3	21 ± 5
O III($\lambda 3444$)	<i>HST</i> /May 14	3439.3 ± 4.3	2.3 ± 0.9	3.1 ± 1.4	21 ± 5
N III($\lambda\lambda 4634, 41, 42$)	AAT/May 11	4638.9 ± 0.9	7.7 ± 0.5	5.2 ± 0.3	26 ± 2
	AAT/May 12	4637.1 ± 1.1	7.3 ± 0.8	5.7 ± 0.7	24 ± 3
	AAT/May 13	4635.7 ± 0.9	11.0 ± 1.0	5.2 ± 0.5	27 ± 2
	<i>HST</i> /May 14	4640.8 ± 0.8	6.3 ± 0.6	3.4 ± 0.4	16 ± 2
He II($\lambda 4686$)	AAT/May 11	4685.0 ± 0.9	4.6 ± 0.5	3.0 ± 0.3	18 ± 3
	AAT/May 12	4686.2 ± 1.1	2.7 ± 0.6	2.0 ± 0.5	11 ± 3
	AAT/May 13	4681.7 ± 0.7	8.5 ± 0.9	4.0 ± 0.4	18 ± 2
	<i>HST</i> /May 14	4686.1 ± 0.9	6.2 ± 0.6	3.3 ± 0.3	21 ± 2

do we expect to see ‘classical’ P Cygni profiles showing absorption and emission in similar strengths. This range of inclinations is around $60\text{--}70^\circ$, in striking agreement with the inclination determined for GRO J1655–40 in quiescence, which adds support to this interpretation. The noise level of our observations prevents distinguishing between such a disc wind and a pure radial outflow, possibly emanating in the inner regions.

5.2 Helium and Bowen fluorescence lines

The only helium line detected in the spectrum is He II Pa ($\lambda 4686$), illustrated in Fig. 6b. There is no detection of He II P β ($\lambda 3203$) or He II Ba ($\lambda 1640$).

We detect three O III Bowen lines, representing both the O1 ($\lambda\lambda 3133, 3444$) and O3 ($\lambda 3407$) cascades (see below). These are shown in Figs. 6c and 6d. Only the line at $\lambda 3133$ is unambiguously detected; this is theoretically expected to be the strongest line of the O1 channel.

There is also emission around 4641 Å (Fig. 6b) which we interpret as primarily due to a blend of three N III Bowen lines ($\lambda\lambda 4634, 41, 42$). It is possible that there is some contribution from the non-Bowen C III lines ($\lambda\lambda 4647, 51, 52$). Our data are of insufficient quality to deblend these lines.

The Bowen fluorescence mechanism as it applies in X-ray binaries has been well discussed from a theoretical standpoint by Deguchi (1985) and in the context of observations of Sco X-1 by Schachter, Filippenko & Kahn (1989). The essence of the mechanism is this: the He II Ly α transition ($\lambda 303.783$) is nearly coincident with two transitions of O III. He II photons can excite these and the subsequent decays, through the O1 and O3 channels respectively, produce UV emission lines of O III. One of these decay transitions, the O4 channel, is in turn nearly coincident with a doublet of N III. This can then be excited and decay to produce N III emission lines. Using the measured line fluxes of the principal related lines we estimate the efficiency of this process, as measured by the Bowen yields.

The oxygen yield is the probability that a He II Ly α photon will produce a cascade through the O1 channel. It is measured by

$$y_{\text{HeO1}} = k_{\text{H}} \frac{f(\lambda 3133)}{f(\lambda 4686)} \quad (1)$$

where $f(\lambda)$ is the *dereddened* line flux. Following Schachter et al. (1989), we adopt $k_{\text{H}} = 0.28$. This value is dependent on the temperature of the producing region, but the uncertainty this introduces is comparable to the uncertainty in the line flux measurements and much less than that in dereddening the flux ratio. Using the Seaton (1979) extinction curve with $E(B - V) = 1.2 \pm 0.1$, we obtain

$$y_{\text{HeO1}} = 0.70 \pm 0.15. \quad (2)$$

Deguchi (1985) predicts values for this yield between 0.5 and 0.8; Schachter et al. (1989) find values ranging from 0.47–0.59. Our results are consistent with these, and are not precise enough to further constrain the emission line region.

In an analogous way, the nitrogen yield, y_{ON} , represents the fraction of O4 photons which produce a nitrogen cascade. The situation is complicated here by two factors. Firstly we are unable to deblend a possible C III component from the N III blend, so we really only have an upper limit on the N III flux. Secondly, to perform this calculation correctly we need to know the strengths of both the O1 and O3 cascades, since both can in turn initiate an O4 cascade. We are unable to reliably measure any O3 lines so we cannot quantify this contribution. If we simply ignore the O3 contribution and define

$$y_{\text{ON}} = k_{\text{KM}} \frac{f(\lambda\lambda 4634, 41, 42)}{f(\lambda 3133)} \quad (3)$$

where $k_{\text{KM}} = 8.6$, independent of physical conditions, then this will also lead to us overestimating the yield. We determine

$$y_{\text{ON}} \leq 3.7 \pm 0.8 \quad (4)$$

Again, this is in reasonable agreement with Schachter et al. (1989) who find $y_{\text{ON}} = 3.2 - 4.0$ for Sco X-1, with the same assumptions; they also note that this is an overestimate.

5.3 A constraint on the extreme ultraviolet flux

We can also use the observed line flux of the He II $\lambda 4686$ line to place an upper limit on the EUV flux. Photoionisation in the disc and/or secondary star by 55–280 eV photons (bounded by the ionisation energy of He II and the carbon K-edge) will produce He III, which will then recombine leading to $\lambda 4686$ emission. We can estimate the EUV flux which will give the observed line emission. This is a very useful constraint, as this region of the spectrum can never be observed directly for a source as highly reddened as GRO J1655–40. Since $\lambda 4686$ could also originate in collisional excitation at the stream impact point, this will be an upper limit. It is also very dependent on the assumed geometry, both of the EUV and line emitting regions. The method has been developed in the context of cataclysmic variables, where the EUV flux is believed to originate at the boundary layer of the disc and white dwarf (Patterson & Raymond 1986, Marsh & Horne 1990). Marsh, Robinson and Wood (1994) demonstrated that it could also be applied to SXTs, with the EUV instead originating from the inner regions of the disc. Their calculation assumes that the EUV radiation is isotropic, appropriate for a point source or a corona. If it originates in the optically thick inner accretion disc then because both the secondary star and the outer disc see these regions at a high inclination, this will substantially overestimate the EUV flux incident upon them. We account for this inclination effect by making a more rigorous assessment of the fraction of EUV luminosity intercepted in both disc and secondary star cases.

This inclination effect introduces a factor of $\cos \theta$ into the EUV angular flux distribution, where θ is the angle of the EUV radiation to the disc normal. We assume that there is no shielding by the inner part of the disc and consider two cases: radiation intercepted by the disc only and radiation intercepted by the secondary star assuming a vanishingly thin disc.

In the disc case the fraction, α , of EUV luminosity intercepted is

$$\alpha \simeq \left(\frac{H}{R}\right)^2 \quad (5)$$

We treat the secondary star case by modelling it as a circle of radius r_{eq} centred on the secondary position. r_{eq} can be determined numerically (as a function of the mass ratio, q) by requiring that the circle subtend the same solid angle at the primary as the real Roche lobe does. For GRO J1655–40 ($q = 2.99$), $r_{eq} = 0.286$, somewhat larger than the polar radius of 0.269. The fraction of flux intercepted is then

$$\alpha \simeq \frac{2r_{eq}^3}{3\pi} \quad (6)$$

We represent the $\lambda 4686$ line luminosity by L_{4686} and the integrated 55–280 eV luminosity by L_{EUV} . A fraction α of the total number of 55–280 eV photons are intercepted by the disc or secondary star and a fraction ϵ of the total number of photoionisations caused by 55–280 eV photons recombine through this channel. For Case B recombination (appropriate when the emission line region is optically thick to the ionising radiation but optically thin to the recombination lines), $\epsilon \simeq 0.2$. The ratio of luminosities will be

$$\frac{L_{\text{EUV}}}{L_{4686}} = \frac{1}{\alpha\epsilon} E_{\text{EUV}} \left(\frac{\lambda_{4686}}{\text{hc}}\right) \quad (7)$$

where E_{EUV} is an average energy of the EUV photons. The EUV flux, F_{EUV} , that we would observe is related to the total luminosity by $F_{\text{EUV}} = L_{\text{EUV}} \cos i / 2\pi d^2$, where d is the distance of the system. For optically thin recombination lines, the line emission will be isotropic. The relation between flux and luminosity then depends only on the fraction, β , of the emission line region that we see: $F_{4686} = \beta L_{4686} / 4\pi d^2$. For a disc, we see one face only and $\beta = 0.5$. For lines originating on the secondary star, β is phase and inclination dependent. The ratio of EUV to line fluxes is

$$\frac{F_{\text{EUV}}}{F_{4686}} = \frac{2 \cos i}{\beta \alpha \epsilon} E_{\text{EUV}} \left(\frac{\lambda_{4686}}{hc} \right) \quad (8)$$

We observe line fluxes in the range $(2.7\text{--}8.5) \times 10^{-15} \text{ erg s}^{-1} \text{ cm}^{-2}$. If these are produced in the disc, then they should be phase independent, and we must interpret this range as due to stochastic variability. We then should use the line flux from May 14 to obtain the best estimate of the May 14 EUV flux. Dereddening this (assuming $E(B - V) = 1.2 \pm 0.1$) and taking $\epsilon = 0.2$, $E_{\text{EUV}} = 100 \text{ eV}$, an EUV bandwidth of 55–280 eV, $\lambda_{4686} = 4686 \text{ \AA}$ and assuming a minimum fractional disc half thickness of $H/R = 0.01$, as was taken by Marsh et al. (1994), this translates into an *upper* limit on the EUV flux per unit frequency interval of $f_\nu (2.4 \times 10^{16} \text{ Hz}) \lesssim 5.9 \times 10^{-24} \text{ erg cm}^{-2} \text{ s}^{-1} \text{ Hz}^{-1}$ for the case where λ_{4686} emission originates only in the disc.

Examining the four line fluxes as a function of orbital phase, however, the flux is highest at spectroscopic phase 0.19, when we see the heated face of the secondary star nearly face on, and lowest at phase 0.81, when we see the rear face of the secondary star. This suggests that the λ_{4686} emission originates at least partially on the secondary star and so this cannot be completely shielded by the disc. With this interpretation we can use the highest λ_{4686} flux, when we see virtually all of the emission region ($\beta \sim 1$) to constrain the EUV flux to be $f_\nu (2.4 \times 10^{16} \text{ Hz}) \lesssim 2.3 \times 10^{-25} \text{ erg cm}^{-2} \text{ s}^{-1} \text{ Hz}^{-1}$.

The latter calculation represents the more realistic limit, in the sense that if the disc did become very thin then the λ_{4686} flux would not become vanishingly small; it would instead be produced on the secondary star. We stress the caveat that we have assumed none of the EUV flux is shielded by the inner disc. If this assumption were invalid then this EUV constraint becomes meaningless.

6 MODELLING THE OPTICAL AND ULTRAVIOLET SPECTRA

We now discuss possible interpretations of the optical/UV spectra. In view of the large uncertainty in determining the intrinsic flux distribution from such highly-reddened spectra, together with the inherent complexity, it would not be appropriate to attempt to fit a detailed model for the complete spectra. Instead we will seek a simple characterisation of the observed spectra and then compare this with the available sources of radiation.

We obtain the best fitting parameters by χ^2 minimisation. Since the scatter about the fit is predominantly due to intrinsic and interstellar features rather than measure-

Table 7. Properties of blackbody fits to the optical and near UV ($\lambda \geq 2600 \text{ \AA}$) *HST* spectra.

	T(K)	A($\times 10^{23} \text{ cm}^2$)
May 14	9800	5.0
June 9	9900	3.4
June 20	9700	3.1
June 30	8900	2.9
July 22	8700	2.2

ment uncertainties, we obtain very large χ^2 values and applying conventional χ^2 confidence region methods leads to unrealistically small error estimates. In line with the simple characterisation approach we therefore do not attempt to construct rigorous confidence limits.

Since we have the most comprehensive wavelength coverage in the first (May) *HST* visit, we will concentrate on modelling that spectrum, noting differences in the other epochs as they arise. We immediately notice that there appear to be two distinct components: a power-law ($\alpha \simeq 0.33$) in the UV and a second component peaking in the optical. The power-law suggests an obvious interpretation as the predicted spectrum of a steady state blackbody accretion disc. The optical component considered in isolation can be characterised by the best-fitting blackbody. The deduced parameters are shown in Table 7 and the fits to the spectra in Fig. 7. This does not give a good fit in detail, but will give us an approximate estimate of the properties of a thermal model. We note in passing that a blackbody does give a better fit to observations than stellar spectra of similar temperatures; the temperatures suggested by the spectra correspond to A stars and hence very large Balmer jumps which we do not see.

Of course to assume that the spectrum longwards of 2600 \AA is purely due to one component is not realistic. The two components will overlap, and whilst the exponential Wien tail of the optical component could drop off rapidly in the UV, it is less clear that the power-law component will drop off so rapidly in the optical. This blackbody characterisation thus represents an upper limit on the size of the optical component. The alternative extreme, to simply extrapolate the power-law into the optical would result in approximately half the flux at the peak of the optical spectrum coming from the power-law. It would not change the position of the peak of the optical component dramatically, so this component should have roughly the same temperature and no less than half the area given in Table 7.

We now move on to consider physical interpretations of these two components in more detail.

6.1 The steady state blackbody disc model

Our first visit G160L data is suggestive of the $\nu^{1/3}$ spectrum expected from a steady state optically thick accretion disc; a similar UV spectral index was found in *HST* observations of X-ray Nova Muscae 1991 (Cheng et al. 1992). While a SXT in outburst is clearly not in a steady state, we might expect this to be a good approximation on the decline from

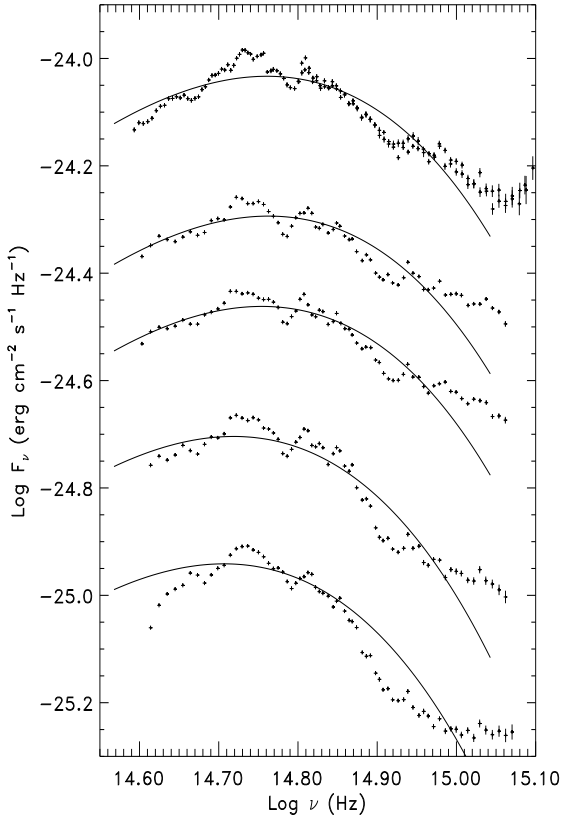


Figure 7. Blackbody fits to the optical excess in the *HST* spectra ($\lambda \geq 2600 \text{ \AA}$). The fits are poor in detail and are only intended to characterise the coarse properties of this component. In order to separate the successive visits clearly, a downward shift of 0.1 has been introduced in each visit relative to the one above it i.e. the lowest visit has been shifted downwards by 0.4.

outburst if the viscous timescale of the disc is shorter than the timescale of mass transfer rate variations. The spectrum in this case is discussed by Frank, King and Raine (1992) and Cheng et al. (1992).

For frequencies, ν , such that

$$kT(R_{out}) \ll h\nu \ll kT(R_{in}) \quad (9)$$

where R_{in} and R_{out} are the radii of the inner and outer edges of the disc and h is Planck's constant, the spectrum reduces to the often referred to $\nu^{1/3}$ disc spectrum:

$$f_\nu = f_0 \frac{\cos i}{d^2} (m\dot{m})^{2/3} \nu_{15}^{1/3} \int_0^\infty \frac{x^{5/3} dx}{e^x - 1} \quad (10)$$

where $f_0 \simeq 2.9 \times 10^{-26} \text{ ergs s}^{-1} \text{ cm}^{-2} \text{ Hz}^{-1}$, i is the inclination, d is the distance in kpc, m is the compact object mass in M_\odot , \dot{m} is the mass transfer rate in $10^{-9} M_\odot \text{ yr}^{-1}$, ν_{15} is the frequency in units of 10^{15} Hz and the integral evaluates to 1.9.

We can fit this spectrum to our data, and with the parameters of Sect. 1.1 deduce a value of $\dot{M} \simeq 8 \times 10^{-7} M_\odot \text{ yr}^{-1}$, adopting our best estimate of background counts and reddening. Allowing the full range of backgrounds and reddening values discussed earlier gives a range

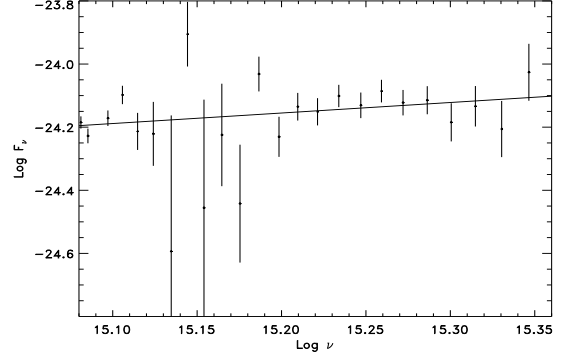


Figure 8. Fit of a $\nu^{1/3}$ spectrum to the rebinned G160L data to determine \dot{M} .

of $1 \times 10^{-7} M_\odot \text{ yr}^{-1} \leq \dot{M} \leq 7 \times 10^{-6} M_\odot \text{ yr}^{-1}$. We can compare this with the Eddington accretion rate of $\dot{M}_{Edd} = 1.6 \times 10^{-7} M_\odot \text{ yr}^{-1}$ (taking a compact object mass of $7 M_\odot$ and assuming an accretion efficiency of 10 per cent. The observed accretion rate (near the peak of the outburst) is thus of the order of the Eddington rate, as might be expected intuitively.

The extrapolation of this spectrum into the extreme UV however would predict $f_\nu (2.4 \times 10^{16} \text{ Hz}) \simeq 1.7 \times 10^{-24} \text{ erg s}^{-1} \text{ cm}^{-2} \text{ Hz}^{-1}$. This exceeds our constraint on the flux at this frequency (see Sect. 5.3) and suggests that either this extrapolation is invalid, or that the assumptions used in deriving the EUV constraint, for example that the inner disc does not obstruct the EUV flux, are inappropriate. We will return to this question in Sect. 8.

6.2 The secondary star contribution

While we could reasonably expect the UV spectrum to be dominated by an accretion disc, in the optical we need to account for the secondary star contribution as well. We first assess the expected contribution if the secondary star spectrum is unaffected by the outburst. In accordance with Orosz & Bailyn (1997) we represent the secondary star contribution using the spectrum of the F5 IV star BD +630013 (Gunn & Stryker 1983). Orosz & Bailyn (1997) present quiescent V band light-curves and estimate that the disc contributes only 5 per cent of this light. Using the phases from Table 2 and the extinction solution of Sect. 4.1 we estimate *secondary star* V band dereddened magnitudes and normalise our secondary star spectrum to this level to obtain a best estimate of the quiescent secondary star contribution for each *HST* visit. The phases and magnitudes are summarised in Table 8.

In Fig. 9 we show the first visit PRISM spectrum before and after subtracting this secondary star component. The optical excess is clearly not removed and so this cannot be accounted for by including a non-irradiated secondary star contribution.

It is likely of course that the secondary star is significantly heated by irradiation during the outburst and that this increases its spectral contribution. If the optical spectrum were dominated by a strongly irradiated secondary star

Table 8. Phases and deduced secondary star magnitudes for each *HST* visit. Photometric phase zero is when the secondary is on the near side of the compact object.

Date	Photometric phase	Quiescent secondary star magnitude (V)	
		observed	dereddened
May 14	0.67	17.08	13.24
June 9	0.38	17.15	13.31
June 20	0.94	17.28	13.44
June 30	0.75	16.98	13.14
July 22	0.05	17.29	13.45

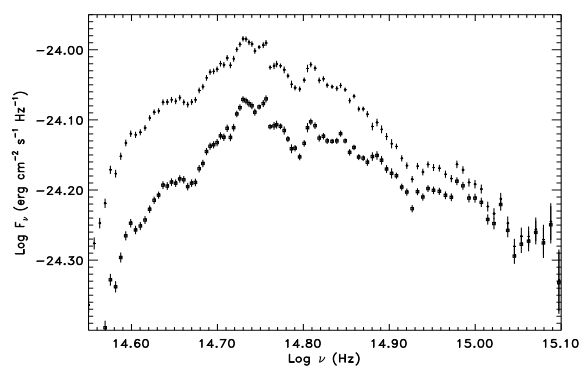


Figure 9. The May 14 PRISM spectrum before and after subtracting an estimate of the *quiescent* spectrum at the same orbital phase.

then we would expect to see an orbital modulation in the light curve, with a maximum at photometric phase 0.5. Figure 10 shows the average flux from a representative continuum region (5600–5700 Å) from each May spectrum plotted on the photometric phase. These data sample the light curve poorly, but do suggest a maximum at phase 0.5. This would be consistent with significant heating of the secondary, but is not conclusive.

Quantitatively an irradiated secondary star model is plausible; the estimated radius of $4.85 R_{\odot}$ (Orosz & Bailyn 1997) corresponds to an average area $\sim 3.6 \times 10^{23} \text{ cm}^2$, although this will be only an upper limit on the visible, irradiated area. Comparison with Table 7 shows that this is a little small, but at least of the right order of magnitude to explain the optical component. We find, however, that the optical excess is seen in all spectra, with a shape largely independent of orbital phase, even for phases for which the irradiated face of the secondary star will not be visible. We must conclude that an irradiated secondary star cannot explain *all* of the excess, but it could provide the phase-dependent part of the solution.

6.3 A warm outer disc?

We next consider if some or all of the excess could be coming from the outer regions of the accretion disc. While we

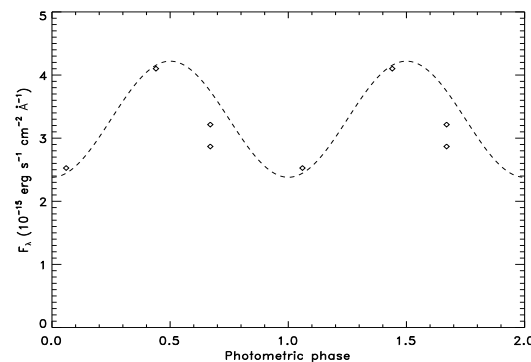


Figure 10. Average 5600–5700 Å fluxes from the May *HST* and AAT spectra plotted on photometric phase. Statistical errors are comparable to or smaller than the symbols. A sine wave with maximum at phase 0.5 has been overplotted to guide the eye; this is not intended to be a model or fit to the data. These are suggestive of such a modulation, but not conclusive.

have already invoked the disc to explain the UV spectrum, this only requires the inner regions of the disc; in that model most (> 80 per cent) of the disc is too cool to make a significant contribution to the UV. We could therefore remove most of the disc, *or give it a completely different temperature distribution*, without destroying our model for the UV spectrum. Two possible ways in which the outer disc temperature distribution are likely to be changed will be considered below. First, however, let us estimate the available area. Adopting a disc radius of 80 per cent of the effective Roche lobe radius (Eggleton 1983) and an inclination of $\sim 70^\circ$, we estimate a projected area of $\sim 2.1 \times 10^{23} \text{ cm}^2$. In addition, we may have to include radiation from the outside edge of the disc since GRO J1655–40 is a high-inclination system. De Jong, van Paradijs and Augusteijn (1996) have found that for some persistent low mass X-ray binaries, the disc half-thickness, H/R can be greater than 0.2. With the inclination of GRO J1655–40 and a disc of this thickness, the projected area of the edge amounts to ~ 70 per cent of the projected area of the disc face, increasing the total area presented by the disc to $\sim 3.6 \times 10^{23} \text{ cm}^2$, comparable to that of the secondary star. As is the case with the secondary, this is of the right order of magnitude to explain the observed radiation.

If thermal emission from the outer disc is responsible for the observed optical component, this would require us to heat these regions up to $\sim 10\,000 \text{ K}$. Is this possible? Qualitatively, this is what we would expect in the presence of a significant irradiating flux. The exact results depend sensitively upon the shape of the concave disc surface, but in general a disc in which energy generation is dominated by irradiation is expected to have a flatter temperature distribution than a steady state disc dominated by viscous dissipation. For example, Vrtilik et al. (1990) derived $T \propto R^{-3/7}$ for the irradiation dominated limit instead of $T \propto R^{-3/4}$. When both dissipation and irradiation are considered, the inner disc will be dominated by dissipation whilst irradiation will raise the temperature of the outer disc above that of a steady state dissipative model. The spectrum expected is then qualitatively similar to that observed except that there is a very

smooth spectral transition between the two regimes (irradiation dominated optical emission and dissipative far-UV) in contrast to the sharp break we observe. It may be that using more realistic local spectra than black bodies and including the effects of limb darkening will explain the sharpness of the break. Limb darkening, in particular, is very strong in the UV (Diaz, Wade & Hubeny 1996), is both temperature and wavelength dependent and can be expected to be significant for a high inclination disc.

Even in the absence of irradiation, there is another mechanism which will cause the temperature distribution in the outer disc to deviate from that of a steady state disc. This is the thermal-viscous limit cycle instability (Cannizzo 1993), in which for a given annulus of the disc, there is a range of effective temperatures for which the annulus is both thermally and viscously unstable. We would not expect any of the disc to lie within this range. The exact temperatures involved are dependent on the disc properties and detailed physics of hydrogen ionisation, but of order 6 000–10 000 K. For most SXTs this is not a problem as it is possible, for plausible mass transfer rates, to have a steady state disc in outburst which is entirely hotter than the unstable temperature range. GRO J1655–40 however, in common with V404 Cyg is a long period system, which means it has a much larger disc than many other SXTs. Because of this, even for a steady state disc accreting at the Eddington rate, part of the outer disc would be cool enough that it should lie within the unstable temperature range: in this Eddington limit case, a temperature of 10 000 K is reached at 0.23 of the primary lobe radius. The implication is then that for GRO J1655–40, there may exist *no globally stable steady state solution with a sub-Eddington accretion rate*. The steady state model *must* therefore break down in the outer disc. What will happen is less clear. The most obvious expectation would be that outside the radius at which the disc is just within the hot stable state there will be an abrupt transition to the cool state. This would imply that most of the disc can never participate in the outburst. Can this really be the case? An alternative that would be consistent with our data is that instead of the outer disc falling into the cool state, it is maintained in the hot state. This would put most of the visible disc (and plausibly also the disc outside edge) at temperatures of $\sim 10\,000$ K and could *quite naturally* explain why the optical component has this temperature and maintains it throughout the outburst.

6.4 Self-absorbed synchrotron emission

Finally we suggest an intriguing alternative to thermal models. Could the cool excess actually be self-absorbed synchrotron emission? This model has more parameters and can give a better fit to the observed spectrum than the black-body model, in particular for the rapid turnover at the peak. Can such a model work quantitatively?

We adopt the simplest possible model for producing this spectrum. We assume a cloud thickness l , area l^2 , volume l^3 . This cloud contains a uniform magnetic field B and a power-law distribution of relativistic electrons, $n_e(E) = \kappa E^{-p}$. For simplicity, we assume equipartition between the magnetic fields and electrons. The expected spectrum is derived by Longair (1994) and we do not reproduce the details. The functional form of the spectrum is:

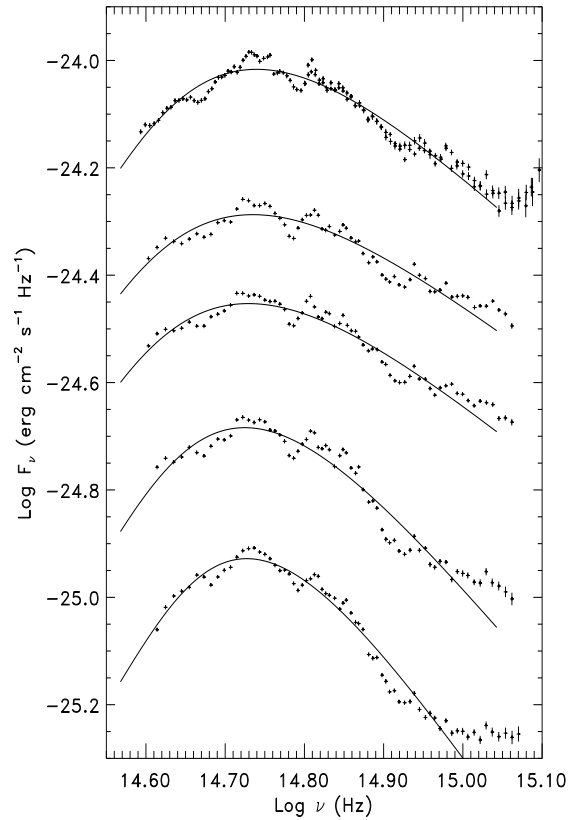


Figure 11. Self-absorbed synchrotron fits to the cool optical excess in the *HST* spectra ($\lambda \geq 2600$ Å). A downward shift has been introduced as in Fig. 7 to separate the successive visits.

$$I_\nu = A\nu^{5/2} [1 - \exp(-B\nu^{(-p+4)/2})] \quad (11)$$

Our problem is then to fit A , B and p and then to determine the underlying physical parameters.

The best fits with such models are shown in Fig. 11 and the deduced parameters are given in Table 9. We immediately note that the source must be very compact. This is actually the best constrained of the parameters as for a self-absorbed synchrotron source, the observed flux depends only on the angular size of the source and the magnetic field. With an estimate of the distance (3.2 kpc) the derived linear size then scales with only the fourth root of the assumed magnetic field.

The clearest evolution in the spectra is the overall decline in flux level; this translates mainly into a shrinking of the inferred synchrotron source. There is also a steepening of the spectrum. This may be due to a change in the electron power-law index, as modelled, or it may be due to a cut-off in the electron distribution above which inverse-Compton and synchrotron losses dominate. Such a cut-off could also contribute to the sharpness of the spectral turnover near 2600 Å.

Synchrotron emission is often considered exclusively a radio phenomenon. That this is not the case is demonstrated by the existence of optical counterparts to extragalactic radio jets. Observations of the other galactic superluminal jet source GRS 1915+105 have, revealed infrared jets, with the

Table 9. Parameters of self-absorbed synchrotron models for *HST* optical and UV data. The Schwarzschild radius of a $7M_{\odot}$ black hole corresponds to 2.1×10^6 cm. In each case, deduced electron energies are $\gamma \sim 50$ – 90 , estimated from the observed synchrotron frequency range of $14.6 \leq \log \nu \leq 15.0$. Electron densities are lower limits obtained by integrating the electron distribution over this energy range.

	p	l (R_{sch})	B (kG)	N_e (10^{12}cm^{-3})
May 14	3.7	97	54	7.6
June 9	3.3	80	61	8.3
June 20	3.4	76	59	8.4
June 30	4.5	70	48	7.8
July 22	5.3	60	42	7.6

same position angle as the radio jets (Sams, Eckart & Sunyaev 1996) and infrared flares with strikingly similar durations, timescales and energies to those seen in the radio at a similar time (Fender et al. 1997). Both of these results are suggestive of infrared synchrotron emission. It has also been suggested that the optical spectrum of the SXT V404 Cyg in quiescence may be dominated by self-absorbed synchrotron emission from an advection dominated accretion flow (Narayan, Barret & McClintock 1997), and that the same is true for GRO J1655–40 (Hameury et al. 1997). Our suggestion is thus speculative but not completely without precedent.

7 MODELLING THE X-RAY SPECTRA

We now move on to consider our X-ray spectra. We constructed composite high-energy spectra covering the ~ 2 – 200 keV region using summed data from the *RXTE* PCA and the BATSE/LAD earth-occultation as described in Sect. 2.4. We were advised by the *RXTE* PCA instrument scientists that the detailed detector calibrations were still evolving, but nonetheless, reasonable fits to the data were obtained in a number of cases, and some basic spectral characteristics of the event could be revealed. We found that for a variety of fitting scenarios, the lowest energy channels ($\lesssim 4$ keV) proved to be problematic in that they contributed significantly to the overall χ^2 . Given the extreme high count rates in these channels, χ^2 values could become untenable very readily, exceeding 100 in some cases. We additionally found channels 49 and 51 to be problematic in some cases, presumably a result of the background estimates used, and we ignored these in our fitting as well.

The general character of the high-energy spectra is that of a power-law with a soft thermal excess component—i.e., the high-soft-state characteristic of black hole candidate X-ray sources accreting at super-Eddington rates. The soft component could be fitted by a multi-colour accretion disc, or equally well by a single temperature blackbody.

Prior to the high-energy ‘turn-on’, i.e., when the source surpassed the BATSE threshold, the PCA spectra required a soft power law (photon index $\Gamma \simeq 3.5$) plus a blackbody with characteristic temperature $T \simeq 0.8$ keV, and an expo-

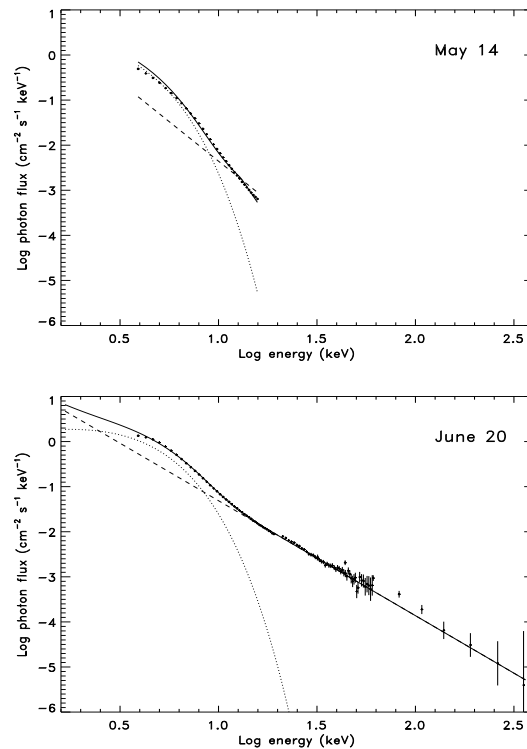


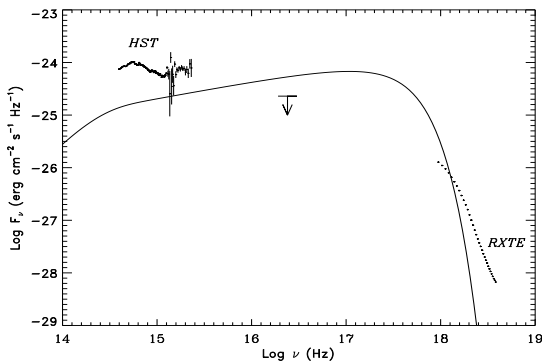
Figure 12. Two component fits to the *CGRO* BATSE and *RXTE* PCA spectra from 1996 May 14 (upper panel) and June 20 (lower panel). The solid line shows the overall fit to the spectrum. The dashed and dotted lines respectively show the power-law and thermal components. In the May 14 spectrum an exponential cut-off has been included in the *overall* fit as described in the text.

ponential cut-off (e-folding scale of 5.4 keV) above $\simeq 13$ keV. The fit to the May 14 spectrum is illustrated in Fig. 12. The background subtracted PCA flux was consistent with zero above ~ 20 keV, consistent with the non-detection by BATSE. The typical χ^2 value obtained were unsatisfactory for the purpose of attributing any one specific model to the data.

At later epochs, although the overall PCA count rates were similar to the initial epochs, the spectrum was harder and the BATSE/LADs could now accumulate sufficient counts to constrain the high energy spectral distribution. By June 20, the joint PCA/BATSE spectrum was modelled as a power-law with photon index $\Gamma \simeq 2.5$ and a $kT \simeq 1.1$ keV blackbody. No high-energy cut-off was required, the power-law now extended to $\gtrsim 100$ keV above which the data become noise limited. In this case, the total reduced χ^2 values obtained were much more reasonable, ~ 2 per degree of freedom. The fit to the June 20 spectrum is illustrated in Fig. 12. It would thus appear that for this outburst, GRO J1655–40 exhibited two distinct substates of the canonical high-soft state characteristic of black hole candidates.

Table 10. Parameters of fits to May 14 and June 20 X-ray spectra.

May 14	Photon index, Γ	3.50 ± 0.05
	Temperature, kT	0.825 ± 0.001 keV
	Column density, N_{H}	3.5×10^{21} cm $^{-2}$
	Cut-off energy	13.0 ± 0.1 keV
	e-fold energy of cut-off	5.4 ± 0.2 keV
	χ^2_{R}	7.168
June 20	Photon index, Γ	2.55 ± 0.02
	Temperature, kT	1.09 ± 0.02 keV
	Column density, N_{H}	8.0×10^{21} cm $^{-2}$
	χ^2_{R}	2.088

**Figure 13.** Composite spectrum for the May 14 observations. Shown are the *HST* spectrum (left), the EUV constraint derived from the He II $\lambda 4686$ flux (centre; see Sect. 5.3) and the *RXTE* spectrum (right). Overlaid is a simplistic model spectrum for a steady state accretion disc accreting at the Eddington rate. This assumes an outer radius of 80 per cent of the Roche lobe and an inner radius of three Schwarzschild radii. No attempt has been made to fit this to the actual data and it is shown only to indicate the simplest expectation for the spectral energy distribution.

8 TOWARDS A CONSISTENT MULTI-WAVELENGTH MODEL FOR THE OUTBURST

Thus far we have dealt with each energy band and observation largely in isolation. In Fig. 13 we show our composite May 14 spectrum. For comparison we have overplotted the spectrum of a steady state disc extending from three Schwarzschild radii to 80 per cent of the Roche lobe. This is a very simplistic model: black body local spectra have been used throughout and no attempt has been made to allow for limb darkening or relativistic effects. The excess seen in the optical can, as described earlier, be attributed to an outer disc heated to hotter than it would be in the steady state model; X-ray irradiation could be causing this. The far UV spectrum could be consistent with a steady state model but the higher energy data are clearly not: the EUV constraint and X-ray spectrum both fall significantly below an extrapolation of the far UV power-law. This makes our interpretation of the far UV spectrum questionable. While we would not expect the X-ray power-law tail to fit this

model, the thermal component is usually attributed to the inner disc and so should represent the X-ray spectrum of the disc. An explanation for the power-law tail (a ubiquitous feature of black hole candidates) has recently been suggested by Titarchuk, Mastichiadis & Kylafis (1996). They propose that it is produced by *bulk motion* Comptonisation from infalling material very close to the black hole event horizon. Their models, whilst still preliminary, predict a power-law spectrum extending to high energies, with the observed spectral index.

Moving on to consider the evolution of the outburst, our most challenging result for such a model to explain is the apparent anti-correlation between optical/UV and hard X-ray behaviour. In the conventional picture of SXT outbursts driven by the limit cycle instability we would expect a fast rise–exponential decay pattern at both optical and X-ray energies (Chen et al. 1997). If reprocessed X-rays dominate the optical energy budget then the problem is even worse, as we would expect the optical output to track the X-ray input closely. How can these difficulties be overcome?

The discrepant X-ray behaviour may be a natural consequence of the long period of GRO J1655–40; most other CVs and SXTs have much shorter periods and smaller discs (although we note that the X-ray transient, V404 Cyg, has a longer period of 6.5 d, but showed an overall X-ray decline, albeit with large superposed variability (Oosterbroek et al. 1997)). The longer period could lead to a longer timescale for the disc to settle into a quasi-steady state and hence a continuing transfer of mass into the inner regions giving the sustained high X-ray fluxes. Detailed modelling of how the limit cycle instability would operate in such a system remains to be done. This may explain why the X-ray activity does not decline as expected. The inverse problem – that irradiation by a high X-ray flux should keep the optical fluxes high – could possibly be explained geometrically. Chen, Livio & Gehrels (1993) considered the secondary shielding the disc from irradiation in their model of the secondary maxima (reflares). It is also true, however, that the effectiveness of irradiation of the disc is greater for a thicker disc as it will intercept more X-ray flux. The shape of the disc is also crucial: we will only have direct irradiation of the disc for a concave surface. Finally the X-ray albedo is likely to be higher if the X-rays fall on the disc at a steep angle of incidence and this will tend to further amplify the dependence on disc thickness and shape. So if the shape and/or thickness of the disc evolves significantly during the outburst, the optical flux could still drop, in spite of the irradiating flux increasing.

As noted in Sect. 6.3, the observed optical spectral evolution could very naturally be explained if a large fraction of the disc is maintained just in the high state, possibly by irradiation. Consider the following scenario. At the beginning of the outburst a heating wave propagates through the disc. If the disc then thins or changes its shape in such a way that the X-ray energy input to a given annulus is decreasing, then a cooling wave will be able to move inwards at the point at which the disc can no longer be maintained in the high state. This would very naturally produce the fixed temperature–shrinking area behaviour inferred. The limit-cycle instability then acts as a thermostat ensuring that the outer edge of the disc stays at a roughly constant temperature. Our observation of this fixed temperature evolution

may therefore be direct evidence that the instability is at work.

It is also worth noting an important difference between this outburst and those previous. Both Bailyn et al. (1995) in the 1994 outburst and Bianchini et al. (1997) during 1995 observed strong Balmer line emission. In contrast we see very little Balmer emission, and broad, shallow, absorption troughs dominate. Bianchini et al. infer from their H α light curves and the changes in the width of the line during the outburst that it was produced by a strong burst of mass transfer at the beginning of the outburst, triggered by the *preceding* hard X-ray rise. That we see no strong Balmer emission in 1996 (when there was only a very slow hard X-ray rise) is consistent with this interpretation and is further evidence that this outburst was qualitatively different to the previous ones. This seems to have been a pure disc outburst with no extra mass transfer from the secondary.

Our alternative suggestion, in which the optical emission is dominated by non-thermal synchrotron radiation has intriguing possibilities. This model could explain why the optical flux seems to be anti-correlated with the hard X-ray flux (which we believe to be *non-thermal* in origin) but appears completely unrelated to the *thermal* soft X-ray flux. The details of such a model are beyond the scope of this paper however.

9 CONCLUSIONS

We have obtained a series of co-ordinated optical, UV and X-ray spectra spanning several months of the outburst of an SXT. Although the optical light curve shows the expected decline, it has a spectrum different to that expected on theoretical grounds. Conversely, although the X-ray spectra showed the familiar high state form, the X-ray fluxes continued to rise through the optical decline, contrary to expectations. We have considered various interpretations of the observations and suggest the following possible scenario:

The outburst was triggered by a heating wave in the disc, causing an optical rise as the outer disc enters the hot state and a soft X-ray rise subsequently when the material starts to reach the inner disc. Inflow to the inner regions continues to rise for some time as the disc tries to find a steady state. About a month after the initial rise the accretion mode near the black hole changes. This results in a rise in the hard X-ray activity and the X-ray variability as the extended hard power-law component becomes prominent. This change is accompanied by a brief radio flare. While the X-ray activity is still rising, the disc itself is changing in thickness and/or geometry so that irradiation becomes less efficient allowing the cooling wave to move inwards producing the drop in optical flux at a nearly fixed temperature. There is also some irradiation of the secondary star, producing an orbital variation in the continuum fluxes and He II 4686 Å emission.

There clearly remain important unanswered questions not only about GRO J1655–40, but about the outbursts of SXTs in general. There are many theoretical avenues to be explored in seeking an explanation of these observations, especially in the modelling of long period, large disc systems and the exploration of non-thermal models for the optical emission.

This work also has many useful lessons for the observer. We have demonstrated the value of co-ordinated, multi-wavelength campaigns in ruling out interpretations which might be suggested by a part of the dataset, but are inconsistent with the whole. We suggest the following priorities for future observations of SXT outbursts:

(i) UV observations are *crucial* to such a campaign for the following reasons. a) It is only in this region that we may be seeing the expected $\nu^{1/3}$ characteristic accretion disc spectrum in this dataset; identification of this is an important indicator of the disc temperature distribution. b) It is in the UV resonance lines that we see the signature of an accretion disc wind. Higher resolution, higher signal to noise observations (possible only for a less extremely reddened source) will test models of accretion disc winds and allow an estimate of the mass loss rate. c) The 2175 Å interstellar absorption feature is our best tool in estimating the reddening of these typically highly reddened objects; other measures such as Na D-lines are not always reliable in these cases. Without a good estimate of the interstellar reddening we cannot determine and hence interpret the intrinsic spectrum.

(ii) The campaign should include spectra, or at least multi-colour photometry, spanning and adequately sampling several consecutive orbits. This will allow us to separate orbital spectral modulations from random variability and distinguish between emission from an irradiated secondary star and the accretion disc. In the event of the discovery of an unambiguously eclipsing SXT these observations would be of central importance, allowing eclipse mapping of the emission regions.

(iii) Comprehensive X-ray spectra spanning as wide an energy range as possible should be an integral part of the campaign. We observe the high energy side of a thermal component, but lower energy coverage is required to accurately characterise this component and distinguish between a single temperature blackbody and a multi-colour disc.

(iv) The campaign should include good red and near infrared coverage to obtain improved characterisation of the long wavelength turnover in the spectrum. This will help in discriminating between thermal and non-thermal emission, which show different long-wavelength limits, and in the thermal case will provide more comprehensive information on the cooler parts of the system.

ACKNOWLEDGEMENTS

RIH is supported by a PPARC Research Studentship. Support for this work was provided by NASA through grant numbers NAG5-3311 and GO-6017-01-94A from the Space Telescope Science Institute, which is operated by the Association of Universities for Research in Astronomy, Incorporated, under NASA contract NAS5-26555 and also through grant NAS5-32490 for the *RXTE* project. This work made use of the *RXTE* and *CGRO* Science Centers at the NASA Goddard Space Flight Center and used the NASA Astrophysics Data System Abstract Service. We acknowledge Alastair Allan's assistance in the AAT observations. Thanks also to Jerome Orosz and Roberto Soria for kindly providing their spectra of GRO J1655–40 for comparison. Thanks to Jeff Hayes, Tony Keyes, Tony Roman and Michael Rosa at STScI for support. RIH would like to thank John Cannizzo,

Phil Charles, Andrew King, Kandu Subramanian and many others for stimulating discussions, and Jean-Pierre Lasota for helpful comments on the manuscript.

REFERENCES

- Bailyn C. D., et al., 1995, *Nat*, 374, 701
 Bianchini A., Della Valle M., Masetti N., Margoni R., 1997, *A&A*, 321, 477
 Bohlin R. C., Savage B. D., Drake J. F., 1978, *ApJ*, 224, 132
 Cannizzo J. K., Chen W., Livio M., 1995, *ApJ*, 454, 880
 Cannizzo J. K., 1993, in Wheeler J. C., ed, *Accretion Disks in Compact Stellar Systems*. World Scientific Publishing, Singapore, p. 318
 Cardelli J. A., Clayton G. C., Mathis J. S., 1989, *ApJ*, 345, 245
 Chen W., Livio M., Gehrels, N., 1993, *ApJ*, 408, L5
 Chen W., Shrader C. R., Livio M., 1997, *ApJ*, 491, 312
 Cheng F. H., Horne K., Panagia N., Shrader C. R., Gilmozzi R., Paresce F., Lund N., 1992, *ApJ*, 397, 664
 Clayton G. C., Hanson M. M., 1993, *AJ*, 105, 1880
 Deguchi S., 1985, *ApJ*, 291, 492; 303, 901
 de Jong J. A., van Paradijs J., Augusteijn T., 1996, *A&A*, 314, 484
 Diaz M. P., Wade R. A., Hubeny I., 1996, *ApJ*, 459, 236
 Ebisawa K., Ogawa M., Aoki T., Dotani T., Takizawa M., Tanaka Y., Yoshida K., 1994, *PASJ*, 46, 375
 Eggleton P. P., 1983, *ApJ*, 268, 368
 Fender R. P. F., Pooley G. G., Brocksopp C., Newell S. J., 1997, *MNRAS*, 290, L65
 Frank J., King A., Raine D., 1992, *Accretion Power in Astrophysics*. Cambridge Univ. Press, Cambridge, pp. 77–9
 Gray D. F., 1992, *The Observation and Analysis of Stellar Photospheres*. Cambridge Univ. Press, Cambridge, p. 431
 Greiner J., Predehl P., Pohl M., 1995, *A&A*, 297, L67
 Gunn J. E., Stryker L. L., 1983, *ApJS*, 52, 121
 Hameury J.-M., Lasota J.-P., McClintock J. E., Narayan R., 1997, *ApJ*, 489, 234
 Hamuy M., Suntzeff N. B., Heathcote S. R., Walker A. R., Gigoux P., Phillips M. M., 1994, *PASP*, 106, 566
 Harmon B. A., et al., 1995, *Nat*, 374, 703
 Harmon B. A., et al., 1992, in Shrader C. R., Gehrels, N., eds, *The Compton Observatory Science Workshop*. NASA CP-3137
 Herbig G. H., 1995, *ARA&A*, 33, 19
 Hjellming R. M., Rupen M. P., 1995, *Nat*, 375, 464
 Hjellming R. M., Rupen M. P., 1996, *IAU Circ.* 6411
 Horne K., 1986, *PASP*, 98, 609
 Horne K., et al., 1996, *IAU Circ.* 6406
 Hunstead R., Campbell-Wilson D., 1996, *IAU Circ.* 6410
 Hunstead R., Wu K., Campbell-Wilson D., 1997, To appear in *Proc. IAU Coll. 163, Accretion Phenomena and Related Outflows*.
 Inoue H., Nagase F., Ishida M., Sonobe T., Ueda Y., 1994, *IAU Circ.* 6063
 Inoue H., Nagase F., Ueda Y. 1995, *IAU Circ.* 6210
 Jahoda K., Swank J. H., Giles A. B., Stark M. J., Strohmayer T., Zhang W., Morgan E. H., 1996, *SPIE*, 2808, 59
 Keyes C. D., Koratkar A. P., Dahlem M., Hayes J., Christensen J., Martin S., 1995, *Faint Object Spectrograph Instrument Handbook*. STScI, p. 52
 Krelowski J., Maszkowski R., Strobel A., 1985, *A&A*, 166, 271
 Lampton M., Margon B., Bowyer S., 1976, *ApJ*, 208, 177
 Lasota J.-P., Narayan R., Yi I., 1996, *A&A*, 314, 813
 Longair M. S. 1994, *High Energy Astrophysics*. Cambridge Univ. Press, Cambridge, pp. 256–262
 Marsh T. R., Horne K., 1990, *ApJ*, 349, 593
 Marsh T. R., Robinson E. L., Wood J. H., 1994, *MNRAS*, 266, 137
 Mineshige S., 1994, *ApJ*, 431, L99
 Mirabel I. F., Rodríguez L. F., 1994, *Nat*, 371, 46
 Motch C., Ilovaisky S. A., Chevalier C., 1985, *SSR*, 40, 219
 Munari U., Zwitter T., 1997, *A&A*, 318, 274
 Nagase F., Inoue H., Kotani T., Ueda Y., 1994, *IAU Circ.* 6094
 Narayan R., Barret D., McClintock J. E., 1997, *ApJ*, 482, 448
 Neckel Th., Klare G., 1980, *A&AS*, 42, 251
 Oosterbroek T. et al., 1997, *A&A*, 321, 776
 Orosz J. A., Bailyn C. D., 1997, *ApJ*, 477, 876
 Orosz J. A., Remillard R. A., Bailyn C. D., McClintock J. E., 1997, *ApJ*, 478, L83
 Orosz J. A., Schaefer B., Barnes S., 1995, *IAU Circ.* 6203
 Patterson, J., Raymond J. C., 1986, *ApJ*, 292, 550
 Remillard R., Bradt H., Levine A., Morgan E., Shirey B., Smith D., 1996, *IAU Circ.* 6393
 Sams B. J., Eckart A., Sunyaev R., 1996, *Nat* 382, 47
 Schachter J., Filippenko A. V., Kahn S. M. 1989, *ApJ*, 340, 1049
 Seaton M. J., 1979, *MNRAS*, 187, 73P
 Shakura N. I., Sunyaev R. A., 1973, *A&A*, 24, 337
 Shlosman I., Vitello P., 1993, *ApJ*, 409, 372
 Shrader C. R., Wagner R. M., Hjellming R. M., Han X. H., Starfield S. G., 1994, *ApJ*, 434, 698
 Tanaka Y., Shibazaki N., 1996, *ARA&A*, 34, 607
 Tavani M., Fruchter A., Zhang S. N., Harmon B. A., Hjellming R. N., Rupen M. P., Bailyn C., Livio M., 1996, *ApJ*, 473, L103
 Tingay S. J., et al. 1995, *Nat*, 374, 141
 Titarchuk L., Mastichiadis A., Kylafis N. D., 1996, *A&AS*, 120, 171
 Tuchman Y., Mineshige S., Wheeler J. C., 1990, *ApJ*, 359, 164
 van der Hooft F., Heemskerk M. H. M., Alberts F. & van Paradijs J., 1998, *A&A*, 329, 538
 Vrtilsek S. D., Raymond J. C., Garcia M. R., Verbunt F., Hasinger G., Kürster M., 1990, *A&A*, 235, 162